



# Quality improvement for high resolution in vivo images by spectral domain optical coherence tomography with supercontinuum source

Maciej Szkulmowski <sup>a,\*</sup>, Maciej Wojtkowski <sup>a</sup>, Tomasz Bajraszewski <sup>a</sup>,  
Iwona Gorczyńska <sup>a</sup>, Piotr Targowski <sup>a</sup>, Wojciech Wasilewski <sup>b</sup>,  
Andrzej Kowalczyk <sup>a</sup>, Czesław Radzewicz <sup>b,c</sup>

<sup>a</sup> *Institute of Physics, Nicolaus Copernicus University, ul. Grudziądzka 517, PL-87-100 Toruń, Poland*

<sup>b</sup> *Institute of Experimental Physics, Warsaw University, ul. Hoża 69, PL-00-681 Warszawa, Poland*

<sup>c</sup> *Institute of Physical Chemistry, Polish Academy of Sciences, ul. Kasprzaka 44/52, PL-01-224 Warszawa, Poland*

Received 15 July 2004; received in revised form 29 October 2004; accepted 4 November 2004

## Abstract

We present a high-resolution spectral domain optical coherence tomography (SDOCT) device with a broad-band supercontinuum light generated in a photonic crystal fiber. The instrument we have developed has an axial resolution of 4  $\mu\text{m}$  in air, a depth of image of 1 mm, and an exposure time of 128  $\mu\text{s}$  per a single A-scan. We adopt and apply two methods for data analysis, which reduce the effects of a strong modulation and temporal fluctuations exhibited by the spectra of supercontinuum. To demonstrate the potential of the methods we show high-resolution SDOCT cross sectional images of the human cornea and retina in vivo.

© 2004 Elsevier B.V. All rights reserved.

*PACS:* 42.30.Wb; 42.66.Ew; 42.66.–p; 07.60.–j; 07.60.Ly; 07.05.Pj

*Keywords:* Optical coherence tomography; Spectral interferometry; Ophthalmology; Image processing

## 1. Introduction

Since 1991 optical coherence tomography (OCT) has been attracting considerable attention as a noncontact and noninvasive method to determine the internal structure of objects that weakly absorb and scatter light. In the OCT technique

\* Corresponding author. Tel.: +48 56 611 3211; fax: +48 56 622 5397.

*E-mail address:* [szkulik@phys.uni.torun.pl](mailto:szkulik@phys.uni.torun.pl) (M. Szkulmowski).

one retrieves the longitudinal scattering intensity profile of an object, from the interference pattern created by the reference and scattered light. Typically, a Michelson interferometer is used, with a reference mirror in one arm and the investigated object in the other arm. In the original approach – time domain OCT (TDOCT) [1] – a single longitudinal scattering profile is obtained by translating the reference mirror. In such a system, both the depth and transversal directions have to be mechanically scanned in order to register a two-dimensional cross-section map of the region of interest within the object. The method has already proved its usefulness in ophthalmology for the diagnosis, staging and monitoring of ocular diseases [2–5] and has been implemented commercially (StratusOCT – Carl Zeiss Meditec Inc., OCT-Ophthalmoscope – Ophthalmic Technologies Inc.).

Spectral domain OCT (SDOCT) [6,7] is an alternative to TDOCT. It provides an almost two orders of magnitude increase in the sensitivity and imaging speed as compared to TDOCT [8–12]. In SDOCT the mechanical depth scan is not required. The reference mirror position is fixed and the spectrum of the light at the output of the Michelson interferometer is recorded with a spectrometer equipped with a high-speed multi-element detector. The Fourier transformation of the interference pattern recorded in such a manner provides the profile of the sample reflectance versus depth (optical A-scan). To obtain two dimensional cross-sectional images additional scanning in a single (transversal) direction is performed.

High speed and low exposure time are especially important in ophthalmic imaging. High speed reduces artifacts due to the eye movements and allows the video-rate as well as 3D registration. The time required to collect the data necessary to reconstruct one line of a tomogram (a single A-scan) is 250  $\mu\text{s}$  in the fastest TDOCT systems with a rapid scanning delay-line [13]. With the SDOCT instrument the same information contained in the spectral fringes can be registered in time as short as 64  $\mu\text{s}$  [14] or even 34  $\mu\text{s}$  [15]. It has been demonstrated [7,8,15] that SDOCT can provide cross-sectional in vivo images of various anatomical details important for clinical diagnostics including

the cornea, corneo-scleral angle, macula lutea and optic disc of the human eye.

The longitudinal resolution in OCT is proportional to the bandwidth of light source used. The source should also provide light with high transversal coherence which facilitates high contrast of spectral fringes. Several types of light sources such as superluminescent laser diodes (SLD) [16,17], femtosecond lasers [12,18], and photonic crystal fibers (PCF) pumped with femtosecond lasers [19,20] have proved their suitability for OCT imaging. It has been recently demonstrated that implementation of the PCF source leads to a sub-micrometric longitudinal resolution [21]. However, it is well known, that supercontinua generated in a PCF exhibit serious spectral modulation and temporal fluctuations that adversely affect the image quality. Several methods such as numerical [22,23] and optical [24] spectral shaping as well as iterative deconvolution [25] have been developed to address the problem of non-Gaussian shape of light spectrum in TDOCT. All numerical methods require the knowledge of the light spectrum and are not practical when the spectrum changes between A-scans.

It was demonstrated that SDOCT has the advantage of providing direct access to the spectral information and to the phase of interference fringes, thus enabling measurements of absorption [26] imaging of blood flow [9,27], and numerical compensation of dispersion [12,17,18]. Therefore, in SDOCT the problem of modulations and temporal fluctuations of interference pattern in OCT device with PCF light source can be resolved in a more convenient way than in TDOCT. As the SDOCT allows for faster measurements, it is also easier to acquire data within a characteristic time-scale of supercontinuum fluctuations.

In this paper, we describe SDOCT instrument combined with a PCF light source. We demonstrate novel implementation of spectral shaping and iterative deconvolution for SDOCT signals, which can be applied even when the source spectrum amplitude fluctuates between A-scans. To test the performance of our SDOCT instrument and the potential of methods improving the resolution of the tomograms we present cross-sectional images of the human cornea and macula in vivo.

## 2. Experimental setup

In our SDOCT instrument (Fig. 1) a supercontinuum (SC) generated in a photonic crystal fiber (PCF) is used as a light source. A train of the femtosecond pulses from a femtosecond Ti:Sapphire laser (4 nJ pulse energy, 40-nm wide spectrum centered at 830 nm, 80 MHz repetition rate) is first compressed in a standard two SF10 prism compressor, attenuated with a half-wave plate and a linear polarizer to about 2nJ, and injected into a 0.5-m long photonic fiber (NL-2-740, Crystal Fibre, Birkerød, Denmark; core diameter 2  $\mu\text{m}$ ). The supercontinuum exiting the fiber is collimated into a beam with a microscope objective. Its spectrum is structured in a way similar to that reported by other groups [19,20]. To avoid undesired eye

exposition to visible and far infrared light dichroic mirrors and filters are inserted into the SC beam. As a result a 120-nm wide (at 10 dB level) band of SC (Fig. 2(a)) is used for OCT imaging.

The supercontinuum beam is launched into a Michelson interferometer and split by a 50/50 non-polarizing cube beam-splitter (Linos) into reference and object arms.

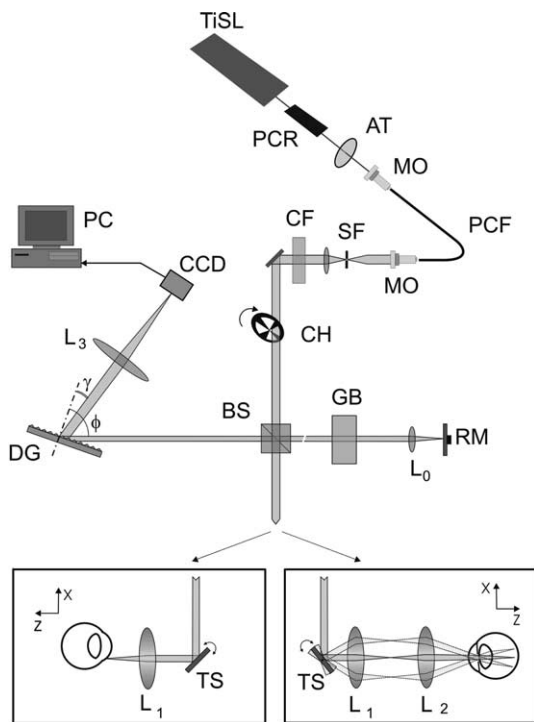


Fig. 1. Optical scheme of the Spectral OCT device: TiSL, Ti:Sapphire laser; PCR, prism compressor; AT, attenuator; MO, objectives; PCF, photonic crystal fiber; SF, spatial filter; CF, color filter; CH, optical chopper; BS, beam splitter; TS, transversal scanner; GB, glass block to compensate dispersion; RM, reference mirror; DG, diffraction grating; CCD, CCD camera; PC, PC computer;  $L_0$ ,  $L_1$ ,  $L_2$ , lenses ( $f = 25.4$  mm);  $L_3$ , lens ( $f = 200$  mm).

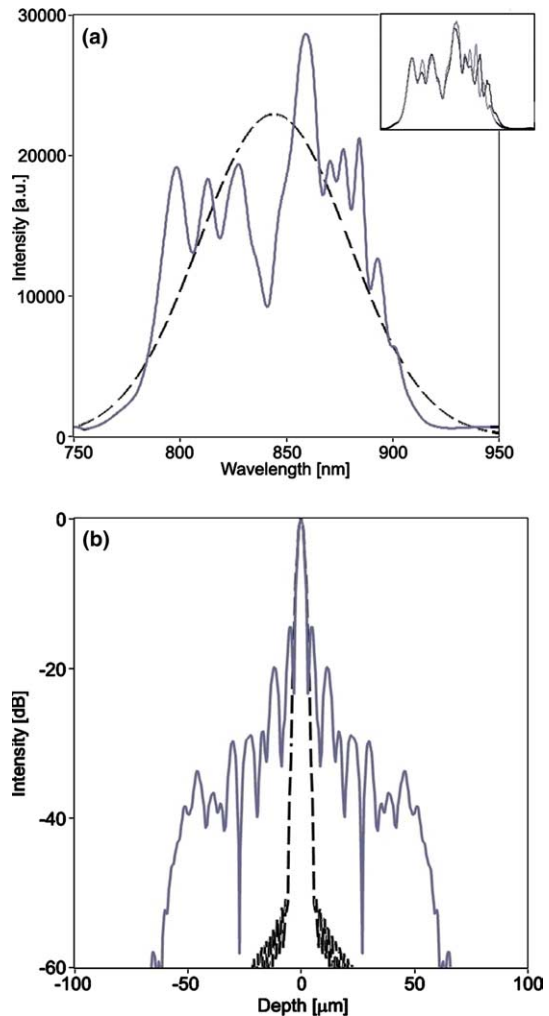


Fig. 2. (a) Spectrum of the supercontinuum generated with PCF source (solid line) and the Gaussian function with the same mean value, standard deviation and area under the curve (dashed line). The inset shows two subsequent spectra registered in 256  $\mu\text{s}$  interval. (b) The absolute values of coherence functions calculated as Fourier transforms of a zero padded (up to 4096 points) spectral shape before (solid line) and after applying the spectral shaping method (dashed line).

The beam in the reference arm is back-reflected by a fixed mirror, while the beam in the other arm is aimed at the object by a transversal scanner. For anterior chamber imaging the galvo-scanner (Cambridge Technology) mirror and the object are placed at the focal points of the lens  $L_1$  ( $f = 2.54$  cm). This ensures that the direction of the analyzing beam is insensitive to the scanning angle. For retinal imaging the parallel beam passes through the telescope ( $1\times$  magnification) constructed with lenses  $L_1$  and  $L_2$  ( $f = 2.54$  cm). The arrangement guarantees that the scanning beam entering the eye at different angles passes through the same point of the pupil. The beam is focused on the retina by the optical system of the eye.

The beam diameter in the focal plane is approximately  $20\ \mu\text{m}$  which determines the transversal resolution. The distance between the adjacent A-scans is about  $1.7\ \mu\text{m}$ . Such oversampling enhances the quality of tomograms due to the effective incoherent speckle averaging. The longitudinal resolution given by the bandwidth of the light source is  $4\ \mu\text{m}$  in air ( $3\ \mu\text{m}$  in tissue).

The object and reference beams are combined on the beam splitter cube and analyzed by a spectrometer, which is equipped with a diffraction grating (1800 grooves/mm, Spectrogon) and a CCD camera (Andor Technology, 1 MHz sampling rate of frame grabber, 16 bit AD conversion,  $1024 \times 128$  pixels,  $27 \times 27\ \mu\text{m}$  pixel size). The total spectrometer efficiency is approximately 10%.

The first line of the 2D CCD sensor of the camera is used to register the spectra while the remaining lines serve as a memory buffer [14]. For the dynamic cross-sectional imaging a single video frame (maximum 128 A-scans) is acquired in 16 ms and transferred to the computer in 160 ms. Static images with wider scanning ranges (larger number of A-scans) are collected proportionally longer. It must be emphasized that in our instrument the patient's eye is exposed to light only during the data collection. For the duration of the data transfer the chopper blocks the beam. In the present design the total illumination time is about 1/10 of the total examination time. An average light power at the cornea is less than  $200\ \mu\text{W}$  during the 16 ms illumination periods (128 A-scans). The total light energy entering

the eye is only 20–40 nJ per single A-scan, far below the European Standard IEC recommendations for maximum cornea exposure for direct viewing [28].

The data is acquired, processed and visualized with a code written in LabView (National Instruments).

### 3. Numerical processing of the data

Spectra collected by the OCT setup described above are evenly sampled in the  $\gamma$ -space, where  $\gamma$  is the diffraction angle. Prior to any processing the spectra are transformed to  $\omega$ -space using the relation,

$$d(\sin \gamma + \sin \phi) = \frac{2\pi c}{\omega}, \quad (1)$$

where  $d$  is the grating constant,  $\phi$  is the angle of incidence (see Fig. 1) and  $c$  is the speed of light. We use linear interpolation to calculate the values of the spectra at the points evenly spaced in  $\omega$ -space as required for fast Fourier transform algorithms.

In SDOCT the recorded signal  $G(\omega)$  is a product of spectrum  $S(\omega)$  of the light source and interference fringes. The fringes originate from the interference of the reference beam (the effective reflectivity of the reference mirror including all losses is  $\beta_0$ ) and the waves reflected at structural layers inside the object (with reflectivity of  $\alpha_k$ ) as well as at the surfaces of optical elements inside both arms of the interferometer (with corresponding reflectivities  $\beta_p$ ):

$$G(\omega) = S(\omega) \left( \sum_k \alpha_k + \beta_0 + \sum_p \beta_p + 2 \sum_{k \neq l} \sqrt{\alpha_k \alpha_l} \cos(\omega \tau_{kl}) + 2 \sum_k \sqrt{\alpha_k \beta_0} \cos(\omega \tau_{k0}) + 2 \sum_{k,p} \sqrt{\alpha_k \beta_p} \cos(\omega \tau_{kp}) + 2 \sum_{p \neq q} \sqrt{\beta_p \beta_q} \cos(\omega \tau_{pq}) \right). \quad (2)$$

The first three terms in the Eq. (2) describe the intensities of the light beams reflected from all interfaces inside the object, the reference mirror and the surfaces of other optical elements in the interferometer, respectively. The following terms represent cross-correlations between these beams. The time delays between any pair of the reflected beams are denoted as  $\tau$  with proper subscripts. The signals reflected from the surfaces of the optical elements inside the Michelson interferometer manifest themselves as a set of horizontal lines running across the tomogram. To eliminate them we perform one additional acquisition with the scanning beam deflected out of the object, what is equivalent to situation where no object is present in the sample arm ( $\alpha_k = 0$ ). This gives a background signal ( $G_b(\omega)$ ),

$$G_b(\omega) = S_b(\omega) \left( \beta_0 + \sum_p \beta_p + 2 \sum_{p \neq q} \sqrt{\beta_p \beta_q} \cos(\omega \tau_{pq}) \right). \quad (3)$$

The background can be subtracted from the signal described by the Eq. (2) provided that the source spectrum in both cases is the same:  $S_b(\omega) = S(\omega)$  (a real situation when the spectrum changes is discussed in Section 3.2). The subtraction yields,

$$G_s(\omega) = S(\omega) \left( \sum_k \alpha_k + 2 \sum_{k \neq l} \sqrt{\alpha_k \alpha_l} \cos(\omega \tau_{kl}) + 2 \sum_k \sqrt{\alpha_k \beta_0} \cos(\omega \tau_{k0}) + 2 \sum_{k,p} \sqrt{\alpha_k \beta_p} \cos(\omega \tau_{kp}) \right). \quad (4)$$

The inverse Fourier transform of the Eq. (4),

$$g_s(\tau) = \Gamma(\tau) \otimes \left( \delta(\tau) \sum_k \alpha_k + 2 \sum_{k \neq l} \sqrt{\alpha_k \alpha_l} \delta(\tau \pm \tau_{kl}) + 2 \sum_k \sqrt{\alpha_k \beta_0} \delta(\tau \pm \tau_{k0}) + 2 \sum_{k,p} \sqrt{\alpha_k \beta_p} \delta(\tau \pm \tau_{kp}) \right), \quad (5)$$

contains Dirac deltas  $\delta$  at positions corresponding to distances between reflecting layers, and the

coherence function of the light  $\Gamma(\tau) = FT^{-1}(S(\omega))$  which determines the axial resolution. Symbol  $\otimes$  denotes the convolution operation. The first term in the Eq. (5) produces a weak signal (to achieve shot noise limited detection, the relations  $\beta_0 \gg \alpha_k$  should be fulfilled) at  $\tau = 0$ , the deltas of the second term are spread within the range  $0 < \tau < n/l/c$  ( $l$  is maximal thickness of the object,  $n$  is the refraction coefficient of the object). The third term resulting from the interference of the object and reference beams contains the essential information on locations of structural interfaces of the object with respect to the reference mirror position. This term can be conveniently moved outside the range  $0 < \tau < n/l/c$  by a proper selection of the position of the reference mirror. Contribution of the fourth term to the interference signal can be ignored because delays  $\tau_{kp}$  are large and produce fringes of high frequencies that are beyond the resolution of the spectrometer.

The individual line of the tomogram is displayed as the modulus  $|g_s(\tau)|$  (in dB scale) of Eq. (5). Such expression is symmetrical with respect to  $\tau = 0$  (i.e., produces mirror images). If the object is thin (like retina or cornea) the resulting mirror images do not overlap. When the object is of considerable thickness (e.g. anterior chamber of the eye) the phase shifting techniques must be applied [14] to remove this artifact.

Because of the way the data are collected, the unprocessed image consists of several blocks, each of a maximum of 128 A-scans. The time separation between adjacent A-scans within one block is a fraction of a millisecond, and no motional artifacts are apparent. The time separation between consecutive blocks is 160 ms which results in small misalignments between them. The adjacent blocks are therefore aligned using an automated matching procedure [29].

### 3.1. Light source spectrum determination

The knowledge of the spectrum of the light source is a prerequisite to apply the resolution improvement methods proposed in the previous contributions [22,23,25] as well as in the present one. Because, as mentioned above, the spectrum of supercontinuum fluctuates in time, the spectral

shape has to be known for each individual A-scan. In our case it is estimated from each individual spectral signal ( $G(\omega)$  and  $G_b(\omega)$ ) as a running average with a Gaussian kernel,

$$\tilde{S}(\omega) = \frac{\int G(\omega')w(\omega - \omega')d\omega'}{\int w(\omega')d\omega'},$$

$$w(\omega) = \exp\left(-\frac{\omega^2}{2\sigma^2}\right). \quad (6)$$

The smoothness of  $\tilde{S}(\omega)$  depends on the adjustable parameter  $\sigma$  determining the width of the Gaussian function. Since the function  $\tilde{S}(\omega)$  is expressed by the convolution of the kernel with the spectral signal, it can be quickly computed by use of the Fourier transformations. The information about the spectral shape is contained in spectral components in the proximity of the central peak. The value of the parameter  $\sigma$  is chosen automatically by finding the distance between the points where the central peak of the inverse Fourier transform of Eq. (2) hides in the noise. This distance, back transformed to the frequency space, gives  $\sigma$ .

### 3.2. Background subtraction and spectral shaping

The Eq. (4) is derived with assumption that both the spectrum shape and the power of the light source do not change between consecutive measurements. If this condition is not fulfilled and the spectral shape of the light source changes between A-scans the following modification is necessary. Prior to subtraction, both signals given by Eqs. (2) and (3) are divided by corresponding light source spectral shapes  $\tilde{S}(\omega)$  and  $S_b(\omega)$ , determined by the procedure described by the Eq. (6). The result of the subtraction is multiplied by an arbitrary shaping function  $S_N(\omega)$ ,

$$G_s(\omega) = S_N(\omega) \left( \frac{G(\omega)}{\tilde{S}(\omega)} - \frac{G_b(\omega)}{S_b(\omega)} \right), \quad (7)$$

where the background signal  $G_b(\omega)$ , is acquired at the end of the measurement as described at the beginning of Section 3.

If the original light source spectrum (generally non-Gaussian) is used as  $S_N(\omega)$  in the background subtracting procedure (Eq. (7)) then the envelope of the coherence function usually exhibits side-

lobes that blur the image and decrease resolution. If  $S_N(\omega)$  is chosen to be a regular smooth function, e.g. Gaussian, with the mean value, standard deviation and area under the curve the same as for  $S(\omega)$  (Fig. 2(a)), then the new coherence function has strongly reduced sidelobes in comparison to the original one (Fig. 2(b)).

It must be noted, that the ratio of original signal  $G(\omega)$  and the source shape  $S(\omega)$  estimated by smoothing does not contain low frequencies. In result, the imaging depth is reduced in proportion to the parameter  $\sigma$ .

Further resolution improvement can be achieved by the use of a deconvolution method described below.

### 3.3. Least square iterative deconvolution

A line of a tomogram (A-scan) obtained under conditions of infinitesimally narrow coherence function is represented by a vector  $\mathbf{d}$  of length  $N$ . Each pixel contains mean reflectance at the depth corresponding to the pixel index. In a real tomogram, the A-scan is described by a vector  $\mathbf{g}$ , which results from the convolution of the vector  $\mathbf{d}$  with the vector  $\Gamma$  representing the coherence function envelope,

$$\mathbf{g} = \Gamma \otimes \mathbf{d}. \quad (8)$$

If the measured vector  $\mathbf{g}$  as well as the coherence function  $\Gamma$  are known, it is possible to find the vector  $\tilde{\mathbf{d}}$  which yields a minimum of the least squares difference between measured and calculated  $\mathbf{g}$ ,

$$J(\tilde{\mathbf{d}}) = (\mathbf{g} - \Gamma \otimes \tilde{\mathbf{d}})^T (\mathbf{g} - \Gamma \otimes \tilde{\mathbf{d}}). \quad (9)$$

The function  $J(\mathbf{d})$  describes a hypersurface in  $N + 1$  dimensional space. The algorithm searches for the minimum of  $J(\mathbf{d})$  in an iterative way, starting from  $\tilde{\mathbf{d}}^0 = 0$ . The subsequent approximations of the minimum are calculated in the direction of the steepest descent,

$$\tilde{\mathbf{d}}^{i+1} = \tilde{\mathbf{d}}^i - \alpha \nabla J(\tilde{\mathbf{d}}^i). \quad (10)$$

Here  $\tilde{\mathbf{d}}^i$  is the result of the  $i$ th iteration,  $\alpha$  is a parameter controlling the step size and  $\nabla$  is a gradient operator. As  $\mathbf{d}$  represents intensities of re-

flected light, any of its negative values are converted to zero in every iteration step. Eq. (10) can be expanded to the following form:

$$\tilde{\mathbf{d}}^{i+1} = \tilde{\mathbf{d}}^i + 2\alpha\Gamma \otimes (\mathbf{g} - \Gamma \otimes \tilde{\mathbf{d}}^i). \quad (11)$$

It is possible to calculate Eq. (11) in the conjugated space, but using as many as six Fourier transformations. However, the number of necessary Fourier transformations may be reduced to two per iteration if Eq. (11) is rearranged to the form:

$$\tilde{\mathbf{d}}^{i+1} = 2\alpha\Gamma \otimes \mathbf{g} + \tilde{\mathbf{d}}^i - 2\alpha\Gamma \otimes \Gamma \otimes \tilde{\mathbf{d}}^i \quad (12)$$

In the above equation the first term is the same in all iterations and can be calculated once per A-scan. The remaining calculations reduce to one convolution of the estimate got from previous iteration with a constant expression  $\Gamma \otimes \Gamma$ . Assuming that the Fourier transform of  $\Gamma \otimes \Gamma$  and the value of  $2\alpha\Gamma \otimes \mathbf{g}$  are obtained once per A-scan, one iteration of Eq. (12) can be calculated using two Fourier transformations and two summations.

To determine  $\alpha$ , the convolution in the Eq. (8) can be regarded as a matrix–vector multiplication,  $\underline{\Gamma}\mathbf{d}$ , where  $\underline{\Gamma}$  is a convolution matrix formed from a vector  $\Gamma$ . The convergence of the Eqs. (10)–(12) is assured if the parameter  $\alpha$  is smaller than the reciprocal of the dominant eigenvalue  $\kappa_{\max}$  of a matrix  $\underline{\Gamma}^T \underline{\Gamma}$  (which corresponds to  $\Gamma \otimes \Gamma$ ) [30],

$$0 < \alpha < \frac{1}{\kappa_{\max}}.$$

For each A-scan the algorithm calculates the dominant eigenvalue  $\kappa_{\max}$  using iterative power method [30]. It must be noted that matrix  $\underline{\Gamma}$  does not need to be explicitly constructed from the vector  $\Gamma$ . The original algorithm of the power method is modified here by replacing the matrix–vector multiplications by two Fourier transformations per iteration. The parameter  $\alpha$  is kept constant during the calculations of vector  $\tilde{\mathbf{d}}$ , Eq. (12).

#### 4. Results

In order to test the performance of the high resolution SDOCT on a biological sample we carried

out measurements on the eye of one of the authors (healthy, 26 years).

The spectral shape of the light source for background signal and A-scans in all images is calculated using Eq. (6) with  $\sigma$  found with the automated method described in Section 3.1.

In Fig. 3 the raw and processed high resolution SDOCT images of the fundus and cornea of the eye in vivo are presented. The strongly reflecting morphological details are white, while those of lower reflectance are shown as darker bands. The raw images (panels a) contain regular horizontal lines introduced by the reflections from the surfaces of optical elements in the interferometer. The lines are discontinuous because the data blocks are already aligned in order to match the structural features that are shifted due to the motion of the eye [29]. The lines are effectively removed with background subtraction procedure given by the Eq. (7) (panels b). It may be noted that the main features both in the retina and the cornea are quite well distinguished. However, the sidelobes resulting from a modulated source spectrum surround each structural interface and cause closely positioned lines to merge. The tomograms in the panels c demonstrate the result of the spectral shaping method. The sidelobes are significantly reduced. The fourth row shows further sidelobes reduction due to the deconvolution method. The retinal pigment epithelium (RPE) and choriocapillary (CC) layers are much better separated than in the original tomogram. The other details are also much sharper.

A standard SDOCT image needs only one Fourier transformation per A-scan. Determination of the spectral shape requires two Fourier transformations per each spectrum and one transformation of the weighting function per whole image (Eq. (6)). The background signal reduction method needs only one additional acquisition per tomogram (with the scanning beam deflected out of the object) and merely direct multiplications and divisions (Eq. (7)). For the spectral shaping method the Gaussian profile should be additionally determined.

In the gradient deconvolution technique the calculations of the step size parameter require

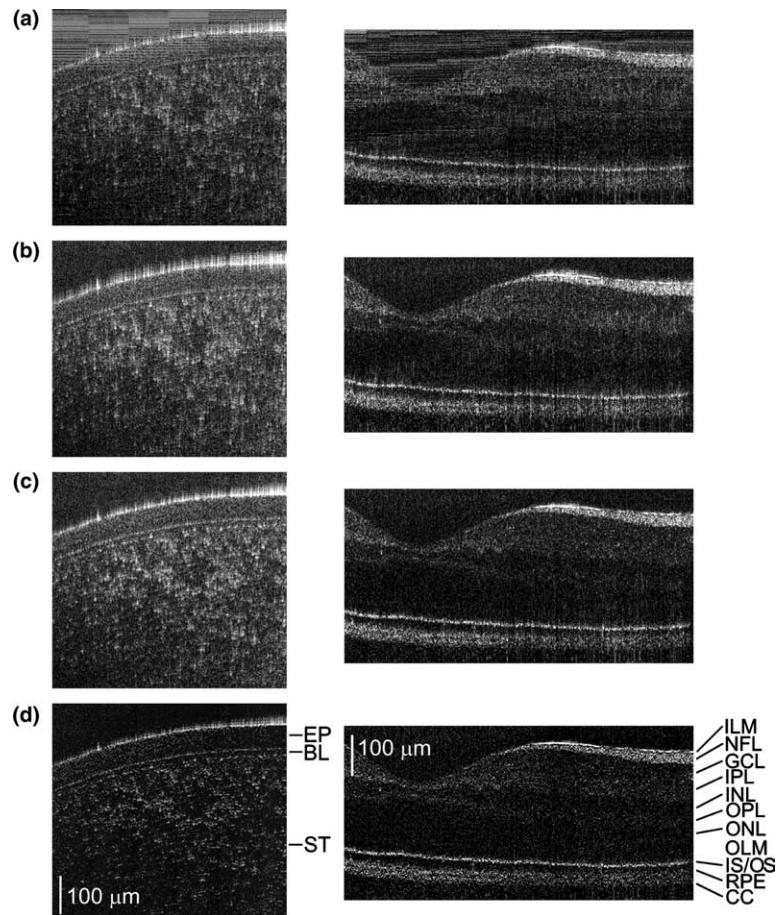


Fig. 3. High resolution ( $3\ \mu\text{m}$  in tissue) SDOCT tomograms of cornea (left, 550 A-scans) and the macula lutea (right, 1450 A-scans) of the normal human eye in vivo. The acquisition time is  $128\ \mu\text{s}$  per A-scan. The raw SDOCT images (a). The tomograms with background removed (b). The images processed using spectral shaping (c) and deconvolution (d) method. The structural elements of the retina: ILM, inner limiting membrane; NFL, nerve fibre layer; GCL, ganglion cell layer; IPL, inner plexiform layer; INL, inner nuclear layer; OPL, outer plexiform layer; ONL, outer nuclear layer; OLM, outer limiting membrane; IS/OS, photoreceptor inner/outer segment junction; RPE, retinal pigment epithelium; CC, choriocapillaries. The structural parts of the cornea: EP, epithelium; BL, Bowmans layer; ST, stroma.

about 60 iterations of the power method per A-scan. Every iteration of the modified method consists of two Fourier transformations. About 300 iterations with two Fourier transformations per iteration (Eq. (12)) are performed for one line of the tomograms presented in Fig. 3.

The total computing time for a single A-scan of the above deconvolution algorithm implemented in LabView software is 40 ms with a standard 3 GHz personal computer.

## 5. Conclusions

We have demonstrated that the Spectral OCT instrument with a Photonic Crystal Fiber supercontinuum light source is capable of high-resolution biomedical imaging. We have also shown that the well known disadvantages of the supercontinuum source, i.e., strong spectral modulation and temporal fluctuations can be effectively reduced by the numerical resolution improvement methods. The improving action of both methods

is the most effective in reducing hair-like structures surrounding strong signals (like air-cornea interface in Fig. 3(a) and (b)).

The algorithms we have used take advantage of the convolution property of Fourier transformation and, therefore, do not need much computation time. Any systematic errors introduced by these procedures do not visibly influence the quality of the image.

The price to be paid for using the original signal for the spectral shape determination is a loss of the imaging depth, inversely proportional to the smoothing parameter  $\sigma$ . In our case, the reduction is about 5% of total imaging range and does not limit the instrument performance.

Neither shaping nor deconvolution measurably change the signal to noise ratio. This due to the relatively low (76 dB) dynamic range of our images which is considerably lower than calculated in [9,10]. However, the dynamic range depends on the optical energy used to acquire one spectrum (illumination time per A-scan multiplied by the power at the cornea). We used the energy which is 100 times lower than that applied in the commercial instrument (20 nJ vs. 2  $\mu$ J per A-scan) and still were able to differentiate all the crucial morphological details in the eye.

## Acknowledgement

This work was supported by grant of the State Committee for Scientific Research KBN 4T11E023 22.

## References

- [1] D. Huang, E.A. Swanson, C.P. Lin, J.S. Schuman, W.G. Stinson, W. Chang, M.R. Hee, T. Flotte, K. Gregory, C.A. Puliafito, J.G. Fujimoto, *Science* 254 (1991) 1178.
- [2] W. Drexler, H. Sattman, B. Hermann, T.H. Ko, M. Stur, A. Unterhuber, Ch. Scholda, O. Findl, M. Wirtitsch, J.G. Fujimoto, A.F. Fercher, *Arch. Ophthalmol.* 121 (2003) 695.
- [3] C.A. Puliafito, M.R. Hee, C.P. Lin, E. Reichel, J.S. Schuman, J.S. Duker, J.A. Izaat, E.A. Swanson, J.G. Fujimoto, *Ophthalmology* 102 (1995) 217.
- [4] M.R. Hee, J.A. Izatt, E.A. Swanson, D. Huang, J.S. Schuman, C.P. Lin, C.A. Puliafito, J.G. Fujimoto, *Arch. Ophthalmol.* 113 (1995) 325.
- [5] W. Drexler, U. Morgner, R.K. Ghanta, F.X. Kärtner, J.S. Schuman, J.G. Fujimoto, *Nat. Med.* 7 (2001) 502.
- [6] A.F. Fercher, C.K. Hitzenberger, G. Kamp, S.Y. El-Zaiat, *Opt. Commun.* 117 (1995) 43.
- [7] M. Wojtkowski, R. Leitgeb, A. Kowalczyk, T. Bajraszewski, A.F. Fercher, *J. Biomed. Opt.* 7 (2002) 457.
- [8] M. Wojtkowski, T. Bajraszewski, P. Targowski, A. Kowalczyk, *Opt. Lett.* 28 (2003) 1745.
- [9] R. Leitgeb, C.K. Hitzenberger, A.F. Fercher, *Opt. Express* 11 (2003) 889.
- [10] J.F. de Boer, B. Cense, B.H. Park, M.C. Pierce, G.J. Tearney, B.E. Bouma, *Opt. Lett.* 28 (2003) 2067.
- [11] M.A. Choma, M.V. Sarunic, C.H. Yang, J.A. Izatt, *Opt. Express* 11 (2003) 2183.
- [12] M. Wojtkowski, V.J. Srinivasan, T.H. Ko, J.G. Fujimoto, A. Kowalczyk, J.S. Duker, *Opt. Express* 12 (2004) 2404.
- [13] A.M. Rollins, M.D. Kulkarni, S. Yazdanfar, R. Ungarunyawee, J.A. Izatt, *Opt. Express* 3 (1998) 219.
- [14] P. Targowski, M. Wojtkowski, A. Kowalczyk, T. Bajraszewski, M. Szkulmowski, I. Gorczyńska, *Opt. Commun.* 229 (2004) 79.
- [15] N.A. Nasiff, B. Cense, M.C. Pierce, S.H. Yun, B.E. Bouma, G.J. Tearney, T.C. Chen, J.F. deBoer, *Opt. Express* 12 (2004) 367.
- [16] T.H. Ko, D.C. Adler, J.G. Fujimoto, D. Mamedov, V. Prokhorov, V. Shidlovski, S. Yakubovich, *Opt. Express* 12 (2004) 2112.
- [17] B. Cense, N.A. Nassif, T.C. Chen, M.C. Pierce, S. Yun, B.H. Park, B.E. Bouma, G.J. Tearney, J.F. de Boer, *Opt. Express* 12 (2004) 2435.
- [18] R.A. Leitgeb, W. Drexler, A. Unterhuber, B. Hermann, T. Bajraszewski, T. Le, A. Stingl, A.F. Fercher, *Opt. Express* 12 (2004) 2156.
- [19] I. Hartl, X.D. Li, C. Chudoba, R.K. Ghanta, T.H. Ko, J.G. Fujimoto, J.K. Ranka, R.S. Windeler, *Opt. Lett.* 26 (2001) 608.
- [20] J.K. Ranka, R.S. Windeler, A.J. Stentz, *Opt. Lett.* 25 (2000) 25.
- [21] B. Povazay, K. Bizheva, A. Unterhuber, B. Hermann, H. Sattmann, A.F. Fercher, W. Drexler, A. Apolonski, W.J. Wadsworth, J.C. Knight, P.St. Russel, M. Vetterlein, E. Scherzer, *Opt. Lett.* 27 (2002) 1800.
- [22] M. Bashkansky, C.W. Duncan, J. Reintjes, P.R. Battle, *Appl. Opt.* 37 (1998) 8137.
- [23] R. Tripathi, N. Nasif, J.S. Nelson, B.H. Park, J.F. de Boer, *Opt. Lett.* 27 (2002) 406.
- [24] A.C. Ackay, J.P. Rolland, J.M. Eichenholz, *Opt. Lett.* 28 (2003) 1921.
- [25] I. Hsu, C. Sun, C. Lu, C.C. Yang, C. Chiang, C. Lin, *Appl. Opt.* 42 (2003) 227.
- [26] R. Leitgeb, M. Wojtkowski, A. Kowalczyk, C.K. Hitzenberger, M. Sticker, A.F. Fercher, *Opt. Lett.* 25 (2000) 820.

- [27] R.A. Leitgeb, L. Schmetterer, C.K. Hitzenberger, A.F. Fercher, F. Berisha, M. Wojtkowski, T. Bajraszewski, *Opt. Lett.* 29 (2004) 171.
- [28] European Standard IEC 60825-1:1993/A2:2001 Safety of laser products, Part 1: Equipment classification, requirements and user's guide.
- [29] T. Bajraszewski, M. Wojtkowski, P. Targowski, M. Szkulmowski, A. Kowalczyk, *Proc. SPIE* 5316 (2004) 226.
- [30] Z. Fortuna, *Numerical Methods*, Wydawnictwa Naukowo-Techniczne, Warszawa, 1993 (in Polish).